The impact of impurities on the spin Hall conductivity in β-W

Oliver L. W. McHugh,[1] Wen Fong Goh,[2] Martin Gradhand,[1] and Derek A. Stewart[3,*]

[1] *H. H. Willis Physics Laboratory, University of Bristol, Bristol, UK*
[2] *Physics Department, University of California at Davis, Davis, CA*
[3] *Western Digital Research Center, San Jose, CA*

(Dated: August 15, 2020)

While the metastable β (A15) phase of tungsten has one of the largest spin Hall angles measured, the origin of this high spin Hall conductivity is still unclear. Since large concentrations of oxygen and nitrogen are often used to stabilize β tungsten, it is not obvious whether the high spin Hall conductivity is due to an intrinsic or extrinsic effect. In this work, we have examined the influence of O and N dopants on the spin Hall conductivity and spin Hall angle of β-W. Using multiple first principles approaches, we examine both the intrinsic and extrinsic (skew scattering) contributions to spin Hall conductivity. We find that intrinsic spin Hall conductivity calculations for pristine β-W are in excellent agreement with experiment. However, when the effect of high concentrations (11 at.%) of O or N interstitials on the electronic structures is taken into account, the predicted intrinsic spin Hall conductivity is significantly reduced. Skew scattering calculations for O and N interstitials in β-W indicate that extrinsic contributions have a limited impact on the total spin Hall conductivity. However, we find that the spin-flip scattering at O and N impurities can well explain the experimentally found spin-diffusion length within the range of 1-5 nm. To explain these findings, we propose that dopants (O and N) help to stabilize β-W grains during film deposition and afterwards segregate to the grain boundaries. This process leads to films of relatively pristine small β-W grains and grain boundaries with high concentrations of O or N scattering sites. This combination provides high spin Hall conductivity and large electrical resistance, leading to high spin Hall angles. This work shows that engineering grain boundary properties in other high spin Hall conductivity materials could provide an effective way to boost the spin Hall angle.

I. INTRODUCTION

While current magnetic RAM devices based on spin-transfer-torque (STT) have demonstrated impressive speed and retention, the power requirement for this technology is still a key challenge for its widespread adoption. This constraint has led to a broad search for alternative switching mechanisms that operate at lower currents. One possible route is to leverage the recently rediscovered spin Hall effect[1–3] in future low power spin-orbit torque (SOT) MRAM devices. In a spin Hall material, the presence of strong spin-orbit interactions will cause an applied electrical current to generate a perpendicular spin current. The ratio between these two currents is given by the spin Hall angle, θ_{SH}. This induced spin current can be used to switch the spin orientation of a neighboring magnetic layer at lower applied currents than those used in STT-MRAM devices. In addition, since the write current never goes through the magnetic tunnel junction, this also results in significant improvements in endurance.

Tungsten in the metastable β phase (A15 phase) has emerged as a leading contender for SOT-MRAM devices[4]. The measured spin Hall angle in β-W (-40%) is much larger than other transition metals (e.g. Pt, Ta). This high spin Hall angle is also surprising, because the spin Hall angle for the stable bcc α phase of tungsten is negligible (<7%). This disparity in spin Hall angles for the different phases has led to recent work[5,6] to resolve the origin of the high spin Hall angle in β-W. Since the growth of β-W requires the addition of O[7–9], N[10,11], F[12,13], or Si[14] impurities to stabilize the crystal lattice, it has been unclear if the high spin Hall angle was intrinsic or extrinsic. The intrinsic spin Hall effect is due to strong relativistic spin-orbit interactions in the material that act to separate spins and produce a transverse spin current when a charge current is applied. The intrinsic component is entirely dependent on the crystal structure and the electronic properties of the perfect crystal and can be calculated using the system Berry curvature[15]. The extrinsic component of the SHE is due to impurities in the system. Spin-dependent or Mott scattering from impurities can also lead to transverse separation of spins within the material. The particular character of the spin-scattering can be further separated into skew-scattering[2,16–18] and side-jump mechanisms[19].

Recent electronic structure calculations[6] have provided support for high intrinsic spin Hall conductivity in pristine β-W due to multiple spin-orbit split bands near the Fermi energy. While these studies have shed light on the electronic structure of pristine β-W, they have not resolved how the stabilizing impurities will affect the electronic structure and overall spin Hall conductivity. The incorporation of oxygen[5] has been demonstrated to increase the spin Hall angle up to $\theta_{SH} = -49\%$. The O and N concentrations used are quite significant ($\sim$12 at.%) and therefore some change in the electronic structure from the pristine A15 tungsten is to be expected. It is also well known that in other materials, like Cu(Bi)[17], skew scattering from impurities can contribute to the spin Hall conductivity. Since multiple dopants can be used to grow the β-W phase, it would also be helpful to identify the optimal dopant for MRAM applications that provides high spin Hall conductivity.

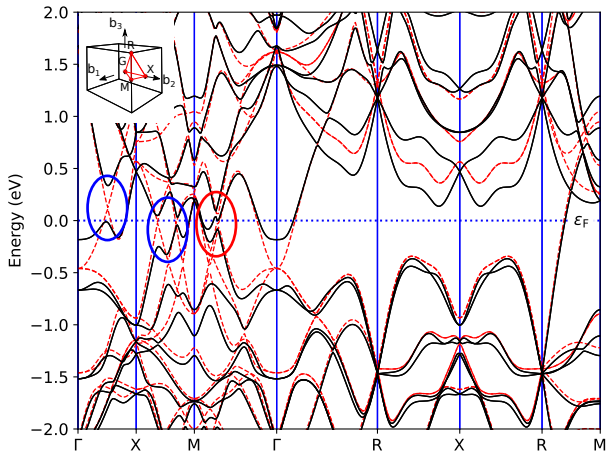

FIG. 1: The band structure of β-W is shown for the cases with (black lines) and without (red dashed lines) spin-orbit interactions. The regions with significant spin-orbit splitting on the Fermi surface are denoted by red circles while spin orbit split bands opening a gap on the Fermi surface are denoted with blue circles.

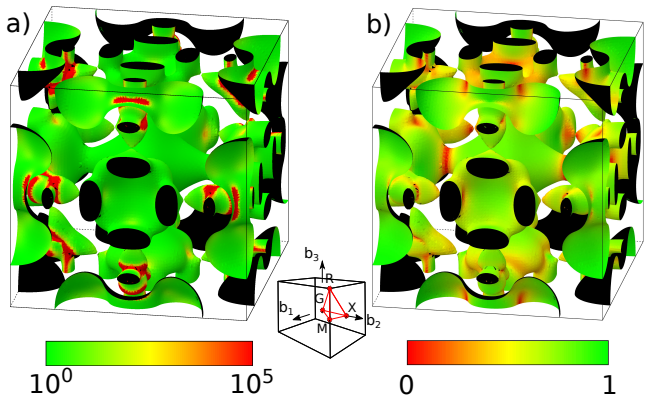

FIG. 2: The Fermi surface of β-W is depicted in the Brillouin zone. a) The colour code shows the Berry curvature (in a.u.) on a logarithmic scale. b) The colour code shows the spin expectation value of the states on the Fermi surface. A schematic of the Brillouin zone and key high symmetry points is noted in the bottom centre.

To help resolve this issue, we have studied the intrinsic and extrinsic contributions to spin Hall conductivity in pristine and doped β tungsten. Using first principle approaches, we can determine the intrinsic spin Hall conductivity due to spin-orbit split bands for both scenarios. In addition, using a Green's function multiple scattering approach[16], we can determine the extrinsic spin Hall conductivity contribution due to skew scattering from dopants (N, O). The *ab-initio* techniques also allow us to determine the optimal positions for different dopants in β-W.

II. SIMULATION APPROACH

We used two distinct approaches to calculate the intrinsic and extrinic component of the SHE. In order to compute the intrinsic component, we used a combination of the plane wave code Quantum Espresso[20] to perform a self-consistent calculation for the pure tungsten system and PAOFlow[21] to subsequently calculate the intrinsic component of the spin Hall conductivity. For consistency, we compare these results to a fully relativistic screened Korringa-Kohn-Rostoker (KKR)[22–24] approach, exploiting the Berry curvature description of the spin Hall conductivity[15,25]. The spin Hall angle can be inferred from those calculations in combination with experimentally measured longitudinal resistivities. The extrinsic contribution to the spin Hall conductivity is determined by combining results from a fully relativistic screened KKR[22–24] approach with the solution of a linearized Boltzmann transport equation.

A. Intrinsic Spin Hall Conductivity Calculations

The electronic structure of pristine β (A15) tungsten in the fully relativistic limit was calculated using the plane wave density functional code Quantum Espresso[20]. For these calculations, we used 60 Ryd and 400 Ryd plane wave cutoffs for the wavefunctions and the charge density, respectively. The exchange and correlation energies were represented in the generalized gradient approximation (GGA). The interactions with ions were described using projector augmented-wave (PAW) pseudopotentials. For the self consistent calculations, a Monkhorst-Pack k-point grid of 12x12x12 was used. The relaxed lattice constant for β-W was found to be 5.089Å. A 24x24x24 Monkhorst-Pack k-point grid was used to generate the tight-binding set of pseudo-atomic orbitals (PAOs) required for subsequent spin Hall conductivity calculations.

In Fig. 1, the band structure calculated using Quantum Espresso is shown for the cases with and without spin-orbit interactions. The spin-orbit split bands near the Fermi level are a strong indicator of significant contributions to the spin Hall conductivity. Pt, the archetype of spin Hall effect materials, has spin-split bands centered at the X and L points[26]. In Fig. 1, it is clearly visible that β-W has a number of regions in the Brillouin zone where spin-orbit split bands occur near the Fermi energy (e.g. along the Γ-X, X-M and the Γ-M lines). The regions marked with blue circles indicated situations where the spin-orbit induced gaps are opening up right at the Fermi level leading to significant contributions in the intrinsic SHC. On the other hand, the region marked with the red circle will give rise to large contributions of the Berry curvature, the source for the SHC, at the Fermi energy, since several spin-orbit split bands cross the Fermi energy. Additional band structure cal-

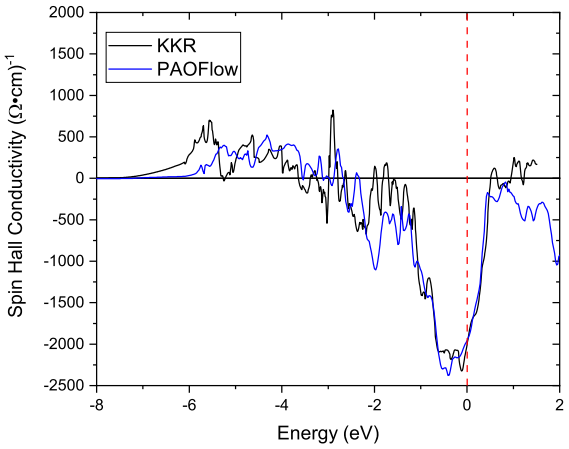

FIG. 3: The calculated spin Hall conductivity for β-W using the KKR formalism[15,25] and the PAOFlow framework[21] (blue line) is shown. The position of the Fermi energy is denoted by a vertical red dashed line.

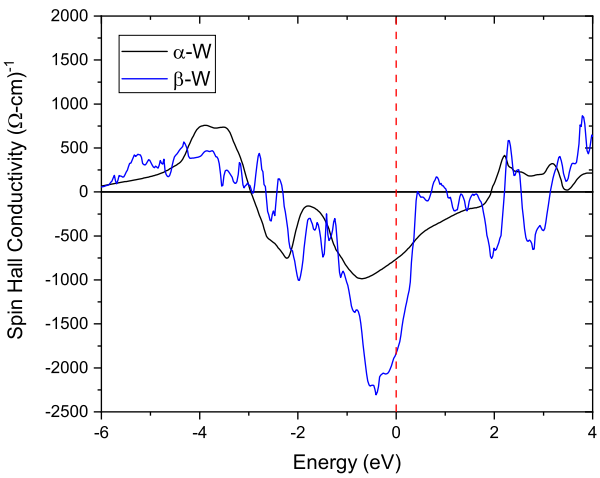

FIG. 4: The intrinsic spin Hall conductivity is shown for pristine α (black line) and β (blue line) tungsten calculated using PAOFlow[21]. The position of the Fermi energy is denoted by a vertical red dashed line.

culations carried out using other approaches (VASP[27,28] (planewave), Questaal[29] (LMTO)) confirm the relativistic band structure predicted by Quantum Espresso.

An examination of the Fermi surface for β-W (Fig. 2) underlines that multiple bands are contributing to conduction. The central electron Fermi surface is made up of a diamond shaped structure that is connected to pyramidal lobes near the Brillouin zone edge. Additional Fermi surface contributions come from pockets centered on the edges of the Brillouin zone. In Fig. 2 a), we use a logarithmic colour scale to show the Berry curvature on the Fermi surface. The Berry curvature peaks dramatically along the Γ-M direction and this peak can be traced to the near degenerate spin-orbit split bands crossing the Fermi energy along Γ-M as indicated by the red circle in Fig. 1. In addition, we provide the spin expectation value of the Bloch states on the Fermi surface. What is shown in practical terms is the expectation value of the $\beta\sigma_z$ operator[60] for one of the two degenerate bands due to the Kramers degeneracy. Here, we chose a gauge in which the off-diagonal elements of the $\beta\sigma_z$ operator vanish. Further details of this approach can be found in Refs.[15,30,31]. In Fig. 2 b), red indicates strong spin mixing induced by near degeneracies in spin-orbit split bands. This spin mixing will lead to reduced contributions in the final SHC since vanishingly small spin angular momentum will be transported. Importantly, regions in the Fermi surface with strong Berry curvature (red regions in Fig. 2 a)) and strong spin mixing (red regions in Fig. 2 b)) do not trivially overlap despite both arising from spin-orbit coupling. This result can partially explain the resulting strong intrinsic SHC as discussed in the following.

The intrinsic SHC is calculated based on the Kubo-Greenwood formalism where the tight-binding set of pseudo-atomic orbitals (PAOs) is constructed with the PAOFlow framework[21]. The electronic wavefunctions generated in Quantum Espresso are first projected onto the PAOFlow atomic orbital basis set. Moving to this light-weight basis set then allows for rapid, high resolution sampling of the Brillouin zone using an adaptive smearing integration scheme developed by Yates et al[32]. The calculated spin Hall conductivity for β-W is shown in Figure 3 in comparison with the KKR results. As can be seen from the figure, the agreement is rather good around the Fermi level especially considering the dramatic difference in the two approaches. Within the KKR method, a localized basis and the local density approximation is used which will lead to a slightly different relaxed lattice constant. The spin Hall conductivity based on the KKR method is calculated using a direct evaluation of the Berry curvature[15,25] which is again fundamentally different from the evaluation of the Kubo formula within PAOFLOW. Since k-point integration in the KKR approach is numerically more demanding, we restricted further calculations of the intrinsic spin Hall conductivity to PAOFlow.

B. Locations of the interstitial impurities

While introducing nitrogen and oxygen into tungsten has been shown to stabilize the β-W phase, little is known about the atomic structure of these doped tungsten systems. A previous study by Sluiter[33] found that nitrogen and oxygen preferred to sit at interstitial sites in the A15 lattice. Given that nitrogen and oxygen atoms are much smaller than tungsten, this is not unexpected. Sluiter ex-

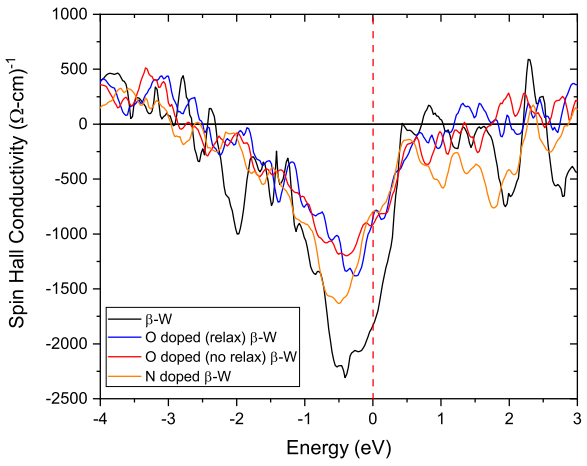

FIG. 5: The calculated spin Hall conductivity is shown for pristine, N doped, and O doped β-W. In addition, we show the result for the O doped system considering structural relaxation. The position of the Fermi energy is denoted by a vertical red dashed line.

amined the energetics of a number of different interstitial positions and found that the position (0.25, 0.25, 0.75) and its symmetry equivalents were the most stable. We have performed structural relaxations for oxygen and nitrogen at various interstitial locations in single unit cells (11 at.% impurity) and 2x2x2 supercells (1.3 at.% impurity) and we also found that this position is the most energetically favourable. The interstitial oxygen or nitrogen also leads to a slight expansion of the β-W lattice constant to 5.165Å and 5.150Å, respectively.

As shown in Fig. 9, the β-W unit cell contains 8 possible interstitial impurity positions. Therefore, there are a total of 8 unique extrinsic spin Hall calculations that must be performed for β-W in order to paint a full picture of the spin and charge dynamics of the impurity system. In α-W, there are 6 interstitial impurity positions (see Fig 8), however most of them are related by symmetry. Considering σ^S_{xy}, the positions 2 and 4 are symmetrically equivalent. The same is true for positions 1 and 6 as well as 3 and 5 where in addition the set (1,6) and (3,5) are related by a rotation of 90° around the z axis.

C. Korringa-Kohn-Rostoker method and Boltzmann transport

The screened KKR method[22–24] was used to calculate the extrinsic component of spin Hall conductivity[16]. Within this method, a real space impurity solver can model the dilute impurity systems without artificial periodic boundary conditions. Due to the localized basis and the fact that the N and O impurities in W are located at interstitial sites, empty spheres had to be placed at the prospective impurity sites during the bulk calculations.

The Green's function of the impurity system contains all the scattering properties of the electronic system required for the semi-classical Boltzmann equation to describe the spin dependent transport[15]. The scattering at impurities, including spin-orbit coupling, gives rise to the impurity induced skew scattering in the limit of dilute impurity concentrations. Within this framework[16], all conductivities are inversely proportional to the impurity concentration, c, which enters the calculations as a parameter only. We can write the conductivity as

$$\sigma = \frac{\sigma|_{c=1at.\%}}{c} \ , \tag{1}$$

where the concentration c is given in at.%. Importantly and in contrast to the calculations for the intrinsic spin Hall conductivities, the Boltzmann approach gives direct access to the longitudinal conductivities as well, allowing for a direct comparison to experimental observations. Furthermore, this implies that the spin Hall angle for the purely skew scattering component is concentration independent. In order to make contact to the experiment, as well as to combine the extrinsic and intrinsic contributions, it is thus crucial to estimate the impurity concentration within the experimental environment. While the character and concentration of different scatterers is often difficult to quantify, our approach is to approximate the concentrations as

$$c = \frac{\sigma^{calc}_{xx}|_{c=1at.\%}}{\sigma^{exp}_{xx}} \ . \tag{2}$$

The resulting concentrations then need to be checked to see if they are within a meaningful range for the considered situation. Throughout this work, we will present extrinsic conductivities at a nominal impurity concentration of 1 at.%, unless we are making direct contact to experiment or if we combine intrinsic and extrinsic contributions, in which case we will explicitly discuss the impurity concentrations considered. It is also important to note that this expression for conductivity is based on scattering from impurities and does not include contributions from other sources such as grain boundaries and interfaces.

III. RESULTS

In this section, we will first discuss the intrinsic and extrinsic contributions to the spin Hall conductivity of α and β-W for various scenarios (pristine, O doped, and N doped). After addressing each contribution individually, we will examine how the total spin Hall conductivity compares with previous theoretical predictions and experimental measurements for relevant dopant concentrations.

A. Intrinsic spin Hall conductivities

The intrinsic SHC for both α and β tungsten is shown in Fig. 4. Both α and β tungsten exhibit negative spin Hall conductivity peaks just below the Fermi energy. As we noted earlier, the high intrinsic spin Hall conductivity in β-W can be related to contributions from several spin-orbit split bands near the Fermi energy. The multiple near degeneracies in this energy range gives rise to rapidly changing positive and negative contributions to the spin Hall conductivity and a great deal of structure in the SHC curve. In the case of α-W, the smaller unit cell leads to a single degeneracy near the Fermi energy situated along the Γ-H symmetry line and a much smoother SHC curve with energy. At the Fermi energy, the intrinsic SHC of α-W is -762 $(\Omega\text{-cm})^{-1}$ and β-W is -1840 $(\Omega\text{-cm})^{-1}$.

In this work, our focus is on the effect of the dopant on the SHC conductivity, commonly used to stabilize the β-W phase. We first calculated the intrinsic spin Hall conductivity for β-W doped at 11 at.% O and N, shown in Fig 5. This composition is equivalent to one O or N per A15 unit cell. This concentration is typical of deposited films used in previous studies.[4,5] In order to investigate the influence of structural relaxation, we include a comparison to a relaxed structure for the case of O doping. As can be seen in Fig. 5, the influence of structural relaxation is marginal, especially around the Fermi energy. In all cases, the peak in the SHC just below the Fermi energy is preserved under doping. However, it is clear that the SHC is significantly reduced. The intrinsic SHC for O doped β-W (-851.139 $(\Omega\text{-cm})^{-1}$) and N doped β-W (-796.62 $(\Omega\text{-cm})^{-1}$) is less than half of the intrinsic SHC (-1840$(\Omega\text{-cm})^{-1}$) for pristine β-W.

B. Alpha-W extrinsic component

While the last section examined the effect of doping on the intrinsic SHC, we did not consider the impact of skew scattering. This is equivalent to investigating the SHC in the dirty limit[34], where the intrinsic contribution typically dominates. In this section, we use a semi-classical Boltzmann formalism to consider the dilute limit.[16] This allows us to access the skew-scattering mechanism as well as the longitudinal conductivities in the dilute impurity limit.

The longitudinal charge conductivities and transverse SHCs for 1 at.% doping of α-W and the resulting spin Hall angles, θ_{SH}, are listed in Tab. I in the appendix. The skew scattering SHAs for N and O impurities at all interstitial positions are similar at around $\theta_{SH} = 1\%$. It should be noted that due to the reduced symmetry induced by the impurity positions 1, 3, 5, and 6 (see Fig. 8 in the Appendix A), the corresponding spin conductivity tensor has a reduced symmetry and will not be perfectly antisymmetric. However, the symmetric part is an order of magnitude smaller than the antisymmetric contribution and averaging over all 4 positions cancels the symmetric part. In Tab. I we present the antisymmetric part only. It is worth noting that the extrinsic SHC due to O and N impurities in α-W is positive and will work against the negative intrinsic SHC.

C. Beta-W extrinsic component

The extrinsic contributions to the conductivity in β-W are much more complex than α-W, containing non-negligible spin and charge conductivities distinct from σ_{xx} and σ^S_{xy}. This is a result of the broken symmetry induced by the impurities in the large A15 structure (see Appendix B). Nevertheless, all impurity positions (empty spheres in the host structure) are related by symmetry operations making the host positions electronically equivalent. As a result of this, considering all different positions, there is an equal number of positive and negative tensor elements for the off-diagonal terms for charge conductivity and for the non-Hall conductivity terms for the spin conductivity. This is highlighted in Fig. 10 in Appendix B.

It is reasonable to assume that O and N in doped β-W systems will randomly occupy the structurally equivalent positions, leading to an equal number of impurities at each interstitial position. In the dilute limit and exploiting Matthiessen's rule, the resulting spin and charge conductivity tensor, σ^s and σ, of a disordered system can be written in terms of the individual conductivity tensors, (σ^s_i, σ_i), as

$$\sigma = \Big(\frac{1}{8}\sum_{i=1}^{8}(\sigma_i)^{-1}\Big)^{-1}. \tag{3}$$

The resulting charge conductivity tensors become diagonal and for N and O impurities, we find charge conductivities $\sigma^N_{xx} = 45.6 \times 10^3$ $(\Omega\text{-cm})^{-1}$ and $\sigma^O_{xx} = 95.2 \times 10^3$ $(\Omega\text{-cm})^{-1}$, respectively. Applying the same process to the spin conductivities, keeping in mind that in principle, the full charge and spin conductivity tensor has to be inverted[35], the resulting SHCs for the N and O impurities are $\sigma^{N,z}_{xy} = -27$ $(\Omega\text{-cm})^{-1}$ and $\sigma^{O,z}_{xy} = -31$ $(\Omega\text{-cm})^{-1}$, respectively.

Finally, the spin Hall angles induced by the skew scattering of the disordered impurity system is $\theta_{\mathrm{N}} = -0.060\%$ for N and $\theta_{\mathrm{O}} = -0.033\%$ for O dopants. Therefore, oxygen and nitrogen incorporation in β-W give extrinsic SHAs with similar and low magnitudes. Notably, they have opposite signs to the extrinsic SHC induced in the α-W system.

D. Spin diffusion length

While the spin Hall angle is important in any charge to spin conversion device, the other equally relevant parameter is the spin diffusion length. It is not only essential in

determining the spin injection and spin transport in the various parts as well as across the interfaces, but in many instances is essential in order to quantify the spin Hall angle in experiments. While the spin diffusion length is such an important parameter, its exact value is often unknown and frequently extracted from complicated fitting procedures of experimental data. The published experimental values range from 1 nm to 5 nm[5,36–43] for a range of resistivities from 0.160×10^{-3} Ω-cm to 0.433×10^{-3} Ω-cm. Within the semi-classical framework, we are able to estimate the spin diffusion length directly from our calculations for N and O impurities in α and β-W. Following Valet and Fert[44], the spin diffusion can be expressed as[45]

$$l_{sf} = \sqrt{\frac{3}{2}} \frac{\pi}{k_F^2 G_0} \sqrt{\frac{\tau_{sf}}{\tau}} \sigma_{xx} \tag{4}$$

where k_F, G_0 , τ_{sf}, τ, and σ_{xx} are the Fermi wavevector, the conductance quantum of $\frac{2e^2}{h}$, the spin-flip scattering time, the momentum relaxation time and the longitudinal charge conductivity, respectively. All parameters are calculated directly from the Boltzmann solver discussed above using the framework introduced previously[46]. In the limit of dilute impurity concentrations, (no scattering due to other sources), all conductivities are inversely proportional to the impurity concentration c as discuss above. The same is also true for the relaxation times, (τ_{sf}, τ), but since they enter the expression in ratio, the concentration dependence cancels out. This implies that the spin diffusion length scales inversely with the concentration in the dilute limit via the conductivity, σ_{xx}. Intuitively, this is reasonable, as the concentration of impurities goes up, scattering increases and the spin diffusion length is reduced. In order to make contact to experiment, we scale the concentration in the calculations to reach the experimental conductivities. For typical resistivities of α-W of 0.2×10^{-3} Ω-cm[4], this implies impurity concentrations of $0.15 - 0.26$ at.%. This is a reasonable finding since rather clean samples are required to grow α-W. On the other hand, in order to reach the experimentally found resistivity for β-W of 0.2×10^{-3} Ω-cm[5], we have to introduce impurity concentrations of 9 and 19 at.% for N and O impurities, respectively. Again, this nicely accounts for the fact that similar concentrations of N and O impurities are crucial in stabilizing β-W. The resulting spin diffusion lengths for α-W and β-W are $l_{sf}^{\alpha} = 5 - 7$ nm and $l_{sf}^{\beta} = 0.9$ nm, respectively. Interestingly, those values are almost independent of the specific impurity character. This underscores the fact that the spin-orbit coupling driving the spin flip relaxation arises from the heavy atomic W.

E. Total Spin Hall Conductivity

To provide a better understanding of the relative importance of the intrinsic and extrinsic contributions to the spin Hall conductivity, the various terms are compared in the bar graph in Fig. 6. For calculations for the extrinsic spin Hall conductivity for α and β-W, it is necessary to specify the concentration of O or N impurities. In the case of α-W (left panel), we have used a dilute concentration of impurities (0.2 at.%) which provides predicted electrical conductivities in good agreement with experiment. For β-W (right panel), we take the same concentration (11 at.%) used to evaluate band structure effects on the intrinsic spin Hall conductivity in O and N doped β-W. This concentration is in the range used to stablize the β-W phase and it also results in predicted electrical conductivities comparable to measured values. The extrinsic spin Hall conductivity of lightly doped α-W is comparable to the intrinsic SHC, but has an opposite sign. This indicates that the total SHC in α-W could be limited to less than 350 $(\Omega\text{-cm})^{-1}$. Of course, for α-W with higher O or N content, the extrinsic SHC contribution will be reduced and the total SHC will approach the intrinsic SHC value. As noted earlier, for β-W, the addition of 11 at.% N or O dopants significantly reduces the intrinsic contribution to the SHC. However, the large contribution of impurities also significant reduces the skew scattering contribution to the SHC and effectively puts this system in the dirty limit for the SHC. In Figure 6, the extrinsic contributions to β-W are two orders of magnitude smaller and listed numerically. This indicates that the extrinsic contribution to the SHC can be safely neglected for β-W.

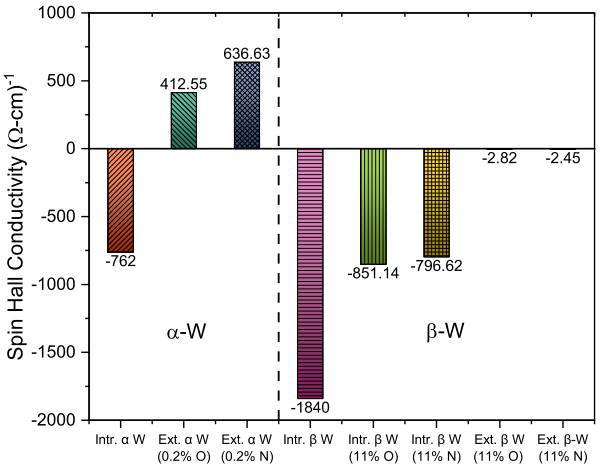

FIG. 6: The predicted intrinsic and extrinsic contributions to the spin Hall conductivity in α and β W is shown. For the case of α-W, the extrinsic spin Hall conductivity is shown for 0.2 at.% O and N doping which provides predicted electrical conductivity in good agreeement with experiment. The intrinsic and extrinsic contributions to spin Hall conductivity in β W for 11 at.% O and N doping is also shown.

It is also helpful to compare our predicted SHC and

spin Hall angles with previous predictions. Our predicted intrinsic spin Hall conductivity for α-W (-762 $(\Omega\text{-cm})^{-1}$) is comparable to the value (-785 $(\Omega\text{-cm})^{-1}$) predicted by Sui *et al*[6] from first principles. However, our predicted intrinsic SHC for pristine β-W (-1840 $(\Omega\text{-cm})^{-1}$) is much closer to that of Derunova *et al.*[47] (-1900 $(\Omega\text{-cm})^{-1}$) than the SHC (-1255 $(\Omega\text{-cm})^{-1}$) reported by Sui *et al*[6]. It is unclear why there is a difference in this case. Both previous works used a Kubo-Greenwood approach where the Bloch wave functions from plane-wave (VASP for Sui *et al*[6]) or localized orbital calculations (FPLO for Derunova *et al*[47]) were mapped onto a tight-binding atomic basis set. The β-W A15 crystal structure is a more open crystal structure than α-W crystal structure and this could make the mapping process to a localized basis set more challenging. The β-W SHC also changes rapidly near the Fermi level and this could lead to some variation in predicted values if there are differences in the predicted lattice constant. However, given our good agreement with Derunova *et al.* and the fact that we have used two different, distinct theoretical approaches (KKR and PAOFlow framework), we are confident that our predicted intrinsic SHC is a reasonable estimate for the intrinsic SHC in β-W.

Additional insight can be gained by comparing our predicted values with SHC values extracted from experiments. Figure 7 shows the extracted SHC versus thickness from various experimental works along with our predicted intrinsic SHC for pristine α-W and β-W and β-W with 11% O. Since interdiffusion or alloying could lead to an effective shift in the Fermi energy, we have also listed the maximum intrinsic SHC predicted in pristine β-W at the peak below the Fermi energy. There are a few things to keep in mind when comparing the results in this figure. Our predicted intrinsic SHC shown in the figure is for the case of a bulk (infinite) crystal of β-W. Spin Hall angle measurements are often done on thin films where surface roughness and interdiffusion at interfaces can lead to additional resistance. Defining the active device region for the spin Hall material and the impact of interfaces can lead to errors in the measured resistivity and estimated SHC. Where possible, spin Hall angle measurements are typically done at several film thicknesses and the ratio of $\theta_{SH}(t)/\theta_{SH}(\infty)$ should vary as $1-\text{sech}(t/l_{sf})$ where t is the film thickness and l_{sf} is the spin diffusion length[48,49]. The spin Hall angle is typically used as a fitting parameter in such analysis and the extracted spin Hall conductivity is determined by multiplying by the measured resistivity. As the film thickness increases, the extracted spin Hall conductivity should approach the bulk limit. The results from Hao *et al*[49] (purple triangles) show this trend and approach our predicted intrinsic SHC in the thick film limit. However this fitting procedure based on film thickness can be challenging in the case of β-W, because in thick films, the A15 crystal structure becomes unstable and decomposes into α-W. This can be seen in the work by Mondal *et al*[41] (black squares) where the transition from β-W to α-W around 5 nm is accompanied by a drop in the SHC to values in the range of our α-W intrinsic prediction. It should be noted that for the case of Pai *et al* (red circles), the estimated SHC for the thick 15 nm α-W film is higher than our predicted value. However, in this work, the authors found no clear signature of spin switching due to spin-orbit torque and only provided an upper limit to the spin Hall angle (< 0.07) based on the accuracy of their measurement. So this value can be treated as an upper estimate. Using a slow deposition procedure, Chen *et al*[42](blue inverted triangle) were able to grow β-W films up to 18 nm and the extracted SHC is close to our predicted range for pristine β-W intrinsic SHC. Some other studies[5,42,50,51] have measured SHC values higher than our upper limit for the intrinsic SHC. One possible explanation for these high values could be due to the ferromagnetic/heavy metal interface spin transmission factor used to determine the intrinsic spin Hall angle. This parameter is difficult to determine accurately and an underestimated spin transmission factor would lead to an overestimate of the intrinsic SHC. Overall, the figure shows that our intrinsic SHC for pristine β-W is in much better agreement with experiments than the intrinsic SHC for β-W with 11% O.

IV. DISCUSSION

These calculations provide important insight into the role of dopants on the spin Hall angle in β-W. Using the calculated intrinsic spin Hall conductivity for pristine β-W and the calculated electrical resistivity due to scattering from O impurities, the intrinsic SHA is estimated to be $\theta_\beta^{int} = -37\%$. For β-W, the experimental SHAs have been reported between -30% and -64%[4,5,37,42,50] in good agreement with our estimated values. This finding suggests that the stabilizing impurities do not have a significant effect on the spin Hall conductivity. This conclusion is supported by the small predicted spin Hall conductivity due to extrinsic skew scattering from 11 at.% O and N interstitials as noted in Figure 6. However, as we have seen, the high concentration of O and N dopants ($\sim$11 at.%) used to stabilize β-W films will also have an impact on the electronic structure and the intrinsic spin Hall conductivity. Figure 7 shows that our predicted intrinsic SHC for pristine β-W is in much better agreement with experiments than the reduced intrinsic SHC for β-W with 11% O. This reduced SHC will also lead to a spin Hall angle that is approximately 50% smaller than that measured experimentally. This leads to a dilemma where the pristine β-W calculations indicate that dopants play no significant role in the SHC and spin Hall angle, while our subsequent calculations including interstitials show a clear effect on SHC and spin Hall angle.

In order to resolve this predicament, it is helpful to consider the properties of β-W films as a function of oxygen content. Demasius *et al*[5] examined how the spin Hall angle and SHC in β-W changed with oxygen concentration (0-38 at.%) for a single film thickness (orange

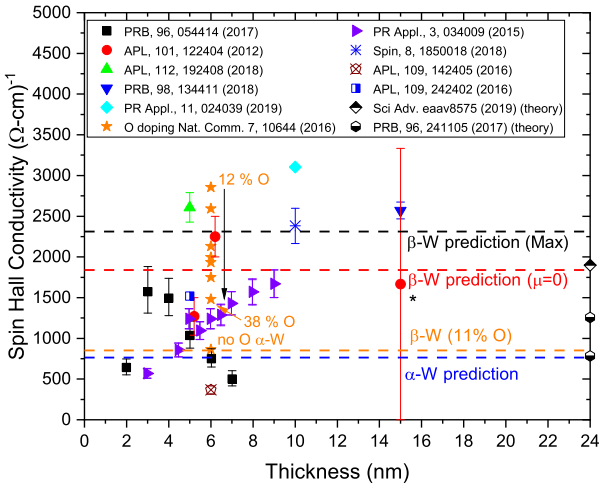

FIG. 7: The magnitude of the Spin Hall conductivity as a function of tungsten film thickness is shown for a variety of experimental measurements[4,5,37,41,42,50–54] and theoretical predictions[6,47]. The calculated bulk intrinsic SHC for pristine β-W is shown at the Fermi energy (red dashed line) and for maximum possible value with p-type doping (black dashed line). The predicted intrinsic SHC for β-W with 11% O doping is also listed (orange dashed line). The calculated bulk intrinsic spin Hall conductivity for α-W is shown with a blue dashed line. Previous intrinsic spin Hall conductivity predictions are noted by half shaded diamond[47] and half shaded hexagons[6] (higher value for β-W and lower value for α-W) at the thick film limit (d=24 nm). Orange stars denote the study by Demasius *et al*[5] that examined the effect of oxygen content on a constant W thickness. The arrow indicates the increase of oxygen content from 12% to 38%.

stars in Figure 7). For W films with no oxygen, the SHC is low and comparable to our predictions for α-W. The SHC then peaks at 12.4 at.% O and steadily declines. The drop in SHC with increasing oxygen concentration is qualitatively similar to our predicted decrease in intrinsic SHC with O or N doping. However, for an uniform distribution of oxygen at concentrations above 11 at.%, this would imply more than one oxygen atom per A15 unit cell. This would lead to significant structural distortion and for such high oxygen concentrations, it is unclear if such a system could still be reasonably called β-W. It is also worth noting that while our predicted intrinsic SHC for β-W with 11 at.% O (1 oxygen per unit cell) is comparable to our predicted value for intrinsic α-W, the extracted SHC for 12.4 at.% O is higher than our predicted intrinsic SHC for pristine β-W. This suggests that the effective dopant concentration in β-W may be less than the measured value. Deposited films are, of course, not ideal crystals and examining how the resistivity and grain size change with O concentration can provide us with some insight into the film structure. In these films, Demasius *et al* found that the resistivity of 12.4 at.% O doped β-W films was only 7% greater than pristine β-W. Overall, the resistivity displays a gradual linear increase with O content up to 25 at.% O. For the case of evenly distributed O or N interstitials in β-W, we would expect a much larger increase in the film resistance. In addition, as the oxygen concentration increases, the measured β-W grain size also decreases from ∼5.5 nm to ∼3 nm. For many metal films, adding oxygen and nitrogen is used to encourage the growth of smaller grains and reduce interfacial roughness. If we assume that the oxygen and nitrogen segregates to the grain boundaries, this could provide one possible explanation for the conflicting results from the intrinsic and the doped β-W spin Hall conductivity calculations.

There is some recent evidence in the literature to support this analysis. Liu and Barmak[10] examined the sputtered deposition of β-W films in the presence of nitrogen gas. They found that the percentage of β-W in the film is directly related to the N_2 pressure using a Langmuir-Freundlich isotherm for N_2 adsorption. They proposed that nitrogen clusters on the surface act as ideal nucleation sites to form W tetrahedra that grow to form CN12 icosahedral triangulated polyhedra. The CN12 icosahedra then coalesce into the A15 crystal structure. The β-W A15 crystal is a Frank-Kasper tetrahederally packed phase[55,56] and the crystal can be viewed as a body centered packing of edge sharing CN12 isosahedra[57]. The high density of N_2 nucleation sites on the surface would also explain the small grain size of β-W compared to α-W. Later work by Barmak and Liu[11] showed that covalent and ionic substrates in general promoted β-W growth in the presence of N_2, while metallic substrates encouraged the formation of the α phase. This suggests that directional N or O bonding at the surface may help in reducing symmetry during tungsten deposition and aid in the formation of the lower symmetry β phase. Symmetry breaking in some form is required to form Frank-Kasper phases in single element materials[58].

Based on this insight, we propose a possible model for spin Hall conductivity in doped β-W. During deposition, the presence of oxygen and nitrogen on the surface helps to stabilize small grains of β-W and prevents the formation of the more energetically favorable α-W. As the film grows, the oxygen and nitrogen interstitials migrate to the grain boundaries, leaving relatively prisitine β-W grains with high intrinsic spin Hall conductivity. A small percentage of O and N may remain within the β-W grains and may slightly reduce the SHC. However, as our calculations show, skew scattering due to these impurities will have a minimal effect on the overall spin Hall conductivity. The oxygen and nitrogen at the grain boundaries act as additional scattering sites for electrons and lead to increased electrical resistance. The role of grain boundaries in the resistance of the β-W films is complex and a subject that warrants further investigations. The traditional Mayades and Shatzkes grain boundary model[?] predicts that the resistance should depend on the electron transmission probability across the grain boundary and scale

inversely with the grain size. Adding additional segregating dopants will simultaneously act to shrink grain size and reduce electron transmission across the grain boundaries. In the work of Demasisus *et al*[5], the resistance for oxygen concentration $< 25\%$ does not scale inversely with grain size, but instead displays a linear trend with dopant concentration. This may indicate that the effect of dopant concentration on grain boundary transmission plays a more dominant role in the electrical resistance than the grain size. Since the spin Hall conductivity is unaffected by grain boundary scattering, the increase in electrical resistance will also lead to an increase in the spin Hall angle with oxygen or nitrogen content. This also indicates that grain boundary engineering could provide one route to tune electrical resistance in spin Hall materials and improve spin Hall angle. This model would work for a range of oxygen or nitrogen concentrations ($<$ 25 %) where the grain boundaries have sufficient capacity to absorb the impurities. The effective O and N concentrations within the grains would also increase (still much less than the total dopant concentration) and this could explain the observed decrease in SHC with oxygen content.

It is important to stress that this theory is one possible explanation for the measured SHC as a function of oxygen concentration. Given the wide range of experimental SHC values for β-W and the limited number of studies that have examined the role of dopant concentration on SHC, it is of course difficult to provide a definitive answer to this issue. Future experiments that examine SHC in β-W as a function of film thickness, grain size, and oxygen or nitrogen content could help in evaluating this model. In addition, characterization studies that could determine the spatial distribution of oxygen or nitrogen in β-W films would also be extremely helpful.

V. CONCLUSION

We have performed a detailed investigation of the influence of O and N dopants on the spin Hall conductivity and angle in β-W. We take into account both intrinsic and extrinsic (skew-scattering) contributions to spin-Hall conductivity. Overall, we find that intrinsic spin Hall conductivity calculations for pristine β-W are in good agreement with experiments. Intrinsic spin Hall conductivity calculations for uniform distribution of 11 at.% O and N interstitials predict a much larger reduction in the spin Hall conductivity than that observed in experiments. Predicted skew scattering for O and N in β-W indicate that this mechanism will have a minimal contribution to spin Hall conductivity and spin Hall angle. Nevertheless, we showed that the induced spin-flip relaxation processes give rise to a spin diffusion length of 0.9nm to 6nm for β-W and α-W, respectively. This is in very good quantitative agreement to experimentally observed values. We propose that O and N helps to stabilize β-W grains during film growth and then segregates to the grain boundaries. This process leads to films of relatively pristine β-W and grain boundaries with high concentrations of O or N scattering sites. This combination provides high spin Hall conductivity and large electrical resistance, leading to high spin Hall angles. Engineering grain boundary properties in other high spin Hall conductivity materials could provide an effective way to boost the spin Hall angle.

Location	σ_{xx} $10^3(\Omega\ \mathrm{cm})^{-1}$	σ^S_{xy} $(\Omega\ \mathrm{cm})^{-1}$	θ (%)
N1	7.8	89	1.14
N2	7.8	72	0.92
N3	7.4	89	1.20
N4	7.8	72	0.92
N5	7.4	89	1.20
N6	7.8	89	1.14
O1	12.9	128	0.99
O2	12.8	126	0.98
O3	12.1	128	1.06
O4	12.8	126	0.98
O5	12.1	128	1.06
O6	12.9	128	0.99

TABLE I: The charge and spin conductivities for α-W with interstitial impurities for both Nitrogen and Oxygen. All conductivities are at 1 at.% impurity concentration.

Acknowledgments

Oliver McHugh gratefully acknowledges scholarship support through the EPSRC funded Centre for Doctoral Training in Condensed Matter Physics and the Western Digital academic program. Wen Fong Goh acknowledges the Western Digital RAMP intern program for supporting his summer research at Western Digital. The authors acknowledge the use of the Fermi surface visualisation tool originally developed by P. Zahn.

APPENDIX A: α-W: DEFINITION OF EMPTY SPHERES AND SUMMARY OF EXTRINSIC RESULTS

The structure of the empty spheres in the α-W structure is shown in Fig. 8 with symmetrically equivalent positions assigned with the same index. The summary of numerical results for all impurity positions is given in Table I, where we show only the antisymmetric part of the spin Hall conductivities as discussed in the main text. The variation between the various positions is marginal and the spin Hall angle is practically constant at 1% across the different positions and O and N impurities.

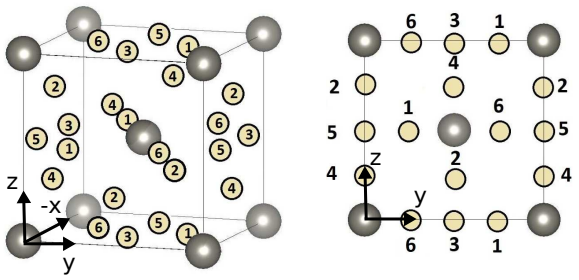

FIG. 8: The locations of the various interstitial atomic positions within the conventional α-Tungsten (gray atoms) unit cell for different orientations are shown labelled 1-6.

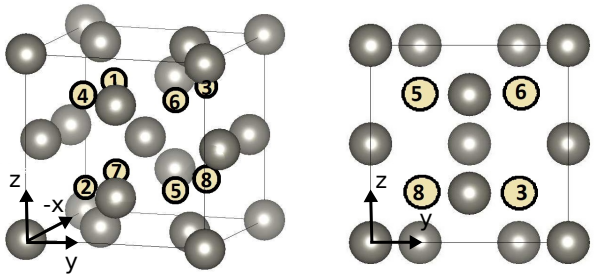

FIG. 9: The positions of the 8 unique interstitial impurity locations for β-W.

APPENDIX B: β-W: DEFINITION OF EMPTY SPHERES AND SUMMARY OF EXTRINSIC RESULTS

The equivalent structural information for β-W is given in Fig. 9. Here are only eight different positions for the empty spheres in the host which are equivalent by symmetry in electronic structure calculations. However, in terms of transport calculations each position breaks separately the symmetry of the crystal which in turn reduces the cubic symmetry relevant for the symmetry of the response tensor. To illustrate this, the spin conductivity for position 1 and 6 in oxygen doped β-W are given by (in units of $(\Omega\text{-cm})^{-1}$)

$$\sigma_1^S = \begin{pmatrix} 8.42 & -31.2 & 25.7 \\ 31.2 & -08.42 & -25.7 \\ -1.82 & 1.82 & 0 \end{pmatrix}, \tag{B1}$$

$$\sigma_6^S = \begin{pmatrix} 8.42 & -31.2 & -25.7 \\ 31.2 & -8.42 & -25.7 \\ 1.82 & -1.82 & 0 \end{pmatrix}, \tag{B2}$$

respectively. For both impurities, the new off-diagonal elements have the same magnitude but show different signs. The same holds for the charge conductivity, where for the oxygen impurity at position 1 and 6, we find (in units of $10^3(\Omega\text{-cm})^{-1}$)

$$\sigma_1 = \begin{pmatrix} 95.2 & 0.41 & -0.14 \\ 0.41 & 95.2 & -0.14 \\ -0.14 & -0.14 & 95.5 \end{pmatrix}, \tag{B3}$$

$$\sigma_6 = \begin{pmatrix} 95.2 & 0.41 & 0.14 \\ 0.41 & 95.2 & 0.14 \\ 0.14 & 0.14 & 95.5 \end{pmatrix}, \tag{B4}$$

respectively. The same pattern (with different signs) holds for N impurities. For the charge conductivity we have summarized this pattern for all impurity positions in Fig. 10 a). Here, red (blue) refers to positive (negative) sign. For all cases, except the xy and yx components, there is an equal number of positive and negative positions which leads to a cancellation of those terms when averaging over all impurity positions. In Fig. 10 we present the same summary for the spin conductivity tensors, where the same argument holds. In all cases considered, the zz component of spin conductivity is 0.

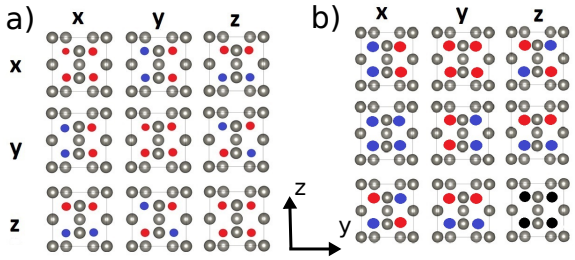

FIG. 10: Signs of the conductivity matrix elements for all impurity positions in β-W. Red refers to a positive sign, blue refers to a negative sign. Here a) is charge conductivity and b) is spin conductivity. The black zz components in the spin conductivity are vanishing.

* derek.stewart@wdc.com

[1] M. I. Dyakonov and V. I. Perel, JEPT Lett. **13**, 467 (1971).
[2] M. I. Dyakonov and V. I. Perel, Phys. Lett. A **35**, 459 (1971).
[3] J. E. Hirsch, Phys. Rev. Lett. **83**, 1834 (1999).
[4] C.-F. Pai, L. Liu, Y. Li, H. W. Tseng, D. C. Ralph, and R. A. Buhrman, Appl. Phys. Lett. **101**, 122404 (2012).
[5] K.-U. Demasius, T. Phung, W. Zhang, B. P. Hughes, S.-H. Yang, A. Kellock, W. Han, A. Pushp, and S. S. P. Parkin, Nat. Commun. **7**, 10644 (2016).
[6] X. Sui, C. Wang, J. Kim, J. Wang, S. H. Rhim, W. Duan, and N. Kioussis, Phys. Rev. B **96**, 241105(R) (2017).
[7] H. Hägg and N. Schönberg, Acta Cryst. **7**, 351 (1954).
[8] G. Mannella and J. O. Hougen, J. Phys. Chem. **60**, 1148 (1956).
[9] S. Basavaiah and S. R. Pollack, J. Appl. Phys. **39**, 5548 (1968).
[10] J. Liu and K. Barmak, Acta Materialia **104**, 223 (2016).
[11] K. Barmak and J. Liu, J. Vac. Sci. Technol. A **35**, 061516 (2017).
[12] C. C. Tang and D. W. Hess, Appl. Phys. Lett. **45**, 633 (1984).
[13] A. J. Narasimham, A. Green, R. J. Matyi, P. Khare, T. Vo, A. Diebold, and V. P. LaBella, AIP Advances **5**, 117107 (2015).
[14] U. Jansson, Appl. Surf. Sci. **73**, 51 (1993).
[15] M. Gradhand, D. V. Fedorov, F. Pientka, P. Zahn, I. Mertig, and B. L. Györffy, J. Phys.: Condens. Matter **24**, 213202 (2012).
[16] M. Gradhand, D. V. Fedorov, P. Zahn, and I. Mertig, Phys. Rev. Lett. **104**, 186403 (2010).
[17] Y. Niimi, Y. Kawanishi, D. H. Wei, C. Deranlot, H. X. Yang, M. Chshiev, T. Valet, A. Fert, and Y. Otani, Phys. Rev. Lett. **109**, 156602 (2012).
[18] J. Sinova, S. O. Valenzuela, J. Wunderlich, C. H. Back, and T. Jungwirth, Rev. Mod. Phys. **87**, 1213 (2015).
[19] L. Berger, Phys. Rev. B **2**, 4559 (1970).
[20] P. Giannozzi, S. Baroni, N. Bonini, M. Calandra, R. Car, C. Cavazzoni, D. Ceresoli, G. L. Chiarotti, M. Cococcioni, I. Dabo, et al., Journal of Physics: Condensed Matter **21**, 395502 (2009).
[21] M. Nardelli, F. T. Cerasoli, M. Costa, S. Curtarolo, R. De Gennaro, M. Fornari, L. Liyanage, A. R. Supka, and H. Wang, Computational Materials Science **143**, 462 (2018).
[22] J. Korringa, Physica **13**, 392 (1947).
[23] R. Zeller, P. H. Dederichs, B. Újfalussy, L. Szunyogh, and P. Weinberger, Phys. Rev. B **52**, 8807 (1995).
[24] L. Peti, S. V. Beide, W. M. Temmer, Z. Szot, G. M. Stocks, and G. A. Gehrin, Philosophical Magazine B **78**, 449 (1998).
[25] M. Gradhand, D. V. Fedorov, F. Pientka, P. Zahn, I. Mertig, and B. L. Györffy, Phys. Rev. B **84**, 075113 (2011).
[26] G. Y. Guo, S. Murakami, T.-W. Chen, and N. Nagaosa, Phys. Rev. Letters **100**, 096401 (2008).
[27] G. Kresse and J. Furthmüller, Comp. Mater. Sci. **6**, 15 (1996).
[28] G. Kresse and J. Furthmüller, Phys. Rev. B **54**, 11169 (1996).
[29] D. Pashov, S. Acharya, W. R. L. Lambrecht, J. Jackson, K. D. Belashchenko, A. Chantis, F. Jamet, and M. van Schilfgaarde, Comp. Phys. Comm. **249**, 107065 (2020).
[30] M. Gradhand, M. Czerner, D. V. Fedorov, P. Zahn, B. Y. Yavorsky, L. Szunyogh, and I. Mertig, Phys. Rev. B **80**, 224413 (2009).
[31] F. Pientka, M. Gradhand, D. V. Fedorov, I. Mertig, and B. L. Györffy, Phys. Rev. B **86**, 054413 (2012).
[32] J. R. Yates, X. Wang, D. Vanderbilt, and I. Souza, Phys. Rev. B **75**, 195121 (2007).
[33] M. H. F. Sluiter, Phys. Rev. B **80**, 220102(R) (2009).
[34] E. Sagasta, Y. Omori, M. Isasa, M. Gradhand, L. E. Hueso, Y. Niimi, Y. .C. Otani, and F. Casanova, Phys. Rev. B **94**, 060412(R) (2016).
[35] G. Bauer, E. Saitoh, and B. J. van Wees, Nature Materials **11**, 391 (2012).
[36] H. L. Wang, C. H. Du, Y. Pu, R. Adur, P. C. Hammel, and F. Y. Yang, Phys. Rev. Lett. **112**, 197201 (2014).
[37] Q. Hao and G. Xiao, Phys. Rev. Applied **3**, 034009 (2015).
[38] S. Cho, S. C. Baek, K.-D. Lee, K. Jo, and B.-G. Park, Sci. Rep. **5**, 14668 (2015).
[39] M. S. Gabor, T. Petrisor Jr., R. B. Mos, A. Mesaros, M. Nasui, M. Belmeguenai, F. Zighem, and C. Tiusan, Journal of Physics D: Applied Physics **49**, 365003 (2016).
[40] N. Behera, P. Guha, D. K. Pandya, and S. Chaudhary, ACS Applied Materials & Interfaces **9**, 31005 (2017), pMID: 28820239.
[41] S. Mondal, S. Choudhury, N. Jha, A. Ganguly, J. Sinha, and A. Barman, Phys. Rev. B **96**, 054414 (2017).
[42] W. Chen, G. Xiao, Q. Zhang, and X. Zhang, Phys. Rev. B **98**, 134411 (2018).
[43] D. Jhajhria, N. Behera, D. K. Pandya, and S. Chaudhary, Phys. Rev. B **99**, 014430 (2019).
[44] T. Valet and A. Fert, Phys. Rev. B **48**, 7099 (1993).
[45] M. Gradhand, D. V. Fedorov, P. Zahn, and I. Mertig, Phys. Rev. B **81**, 245109 (2010).
[46] M. Gradhand, D. V. Fedorov, P. Zahn, and I. Mertig, Phys. Rev. B **81**, 020403(R) (2010).
[47] E. Derunova, Y. Sun, C. Felser, S. S. P. Parkin, B. Yan, and M. N. Ali, Science Advances **5** (2019).
[48] L. Liu, T. Moriyama, D. C. Ralph, and R. A. Buhrman, Phys. Rev. Lett. **106**, 036601 (2011).
[49] Q. Hao and G. Xiao, Physical Review Applied **3**, 034009 (2015), ISSN Physical Review Applied.
[50] W. Skowroński, L. Karwacki, S. Ziętek, J. Kanak, S. Łazarski, K. Grochot, T. Stobiecki, P. Kuświk, F. Stobiecki, and J. Barnaś, Phys. Rev. Applied **11**, 024039 (2019).
[51] Y. Takeuchi, C. Zhang, A. Okada, H. Sato, S. Fukami, and H. Ohno, Applied Physics Letters **112**, 192408 (2018).
[52] L. Neumann, D. Meier, J. Schmalhorst, K. Rott, G. Reiss, and M. Meinert, Applied Physics Letters **109**, 142405 (2016).
[53] H. Mazraati, S. Chung, A. Houshang, M. Dvornik, L. Piazza, F. Qejvanaj, S. Jiang, T. Q. Le, J. Weissenrieder, and J. Akerman, Applied Physics Letters **109**, 242402 (2016).
[54] R. Bansal, G. Nirala, A. Kumar, S. Chaudhary, and P. K. Muduli, SPIN **08**, 1850018 (2018).
[55] F. C. Frank and J. C. Kasper, Acta Crystallogr. **11**, 184 (1958).
[56] F. C. Frank and J. C. Kasper, Acta Crystallogr. **12**, 483 (1959).
[57] M. Engel, P. F. Damasceno, C. L. Phillips, and S. C.

Glotzer, Nature Mater. **14**, 109 (2015).
[58] S. Lee, C. Leighton, and F. S. Bates, Proceedings of the National Academy of Sciences **111**, 17723 (2014).
[59] A. F. Mayadas and M. Shatzkes, Phys. Rev. B **1**, 1382 (1970).
[60] This operator is the spin operator in z direction for the 4 component Dirac equation. The σ_z operator is the conventional third Pauli matrix and β is a 4×4 matrix with entries of 1 for the upper diagonal elements and -1 for lower two diagonal elements. All other elements are zero.